Microstructure Evolution During the Thermal Decomposition of Nickel Oxalate Dihydrate in Air

Alexander A. Matvienko *, Andrey S. Skrypnik, Pavel A. Gribov, Ulanbek K. Mamytbekov, Mustafa M. Kidibaev, Anatoly A. Sidelnikov

Posted Date: 17 March 2026

doi: 10.20944/preprints202603.1297.v1

Keywords: thermal decomposition of precursors; pseudomorph; microstructure; fracture; diffusion-controlled pore growth

 doi:10.20944/preprints202603.1297.v1

Article

Microstructure Evolution During the Thermal Decomposition of Nickel Oxalate Dihydrate in Air

Alexander A. Matvienko [1,2,*], Andrey S. Skrypnik [1], Pavel A. Gribov [1], Ulanbek K. Mamytbekov [2], Mustafa M. Kidibaev [2] and Anatoly A. Sidelnikov [1]

[1] Institute of Solid State Chemistry and Mechanochemistry SB RAS, Kutateladze Str. 18, 630128 Novosibirsk, Russia

[2] Institute of Physics, NAS KR, Chui Avenue, 265-a, 720071, Bishkek, Kyrgyz Republic

* Correspondence: matvienko67@gmail.com; Tel: +996220011901

Abstract

This work presents a comprehensive investigation of the thermal decomposition of nickel oxalate dihydrate as a precursor for the synthesis of porous NiO, with particular emphasis on microstructural formation and evolution. The transformations occurring at successive stages of the reaction were examined using SEM, TEM, N_2 adsorption, TG–DSC–MS, and in situ powder XRD, enabling the mechanisms of pore formation to be elucidated. The decomposition results in the formation of a porous pseudomorph composed of NiO nanoparticles with an average size of approximately 4 nm. The resulting microstructure exhibits hierarchical porous architecture. During dehydration, macropores are generated as a result of crystal fragmentation into blocks several hundred nanometers in size. Subsequent oxalate decomposition leads to the formation of mesoporous aggregates composed of nanometer-sized particles. The factors governing the parameters of the porous microstructure are analyzed. Owing to its hierarchical pore system, the obtained NiO demonstrates significant potential for applications in heterogeneous catalysis, gas sensing, electrodes for super-capacitors and Li-ion batteries, and photoelectrochemical devices. In such systems, macropores facilitate mass transport by reducing diffusion resistance, while mesopores provide a high accessible surface area for adsorption and catalytic reactions.

Keywords: thermal decomposition of precursors; pseudomorph; microstructure; fracture; diffusion-controlled pore growth

1. Introduction

Porous materials based on nickel oxide (NiO) have attracted considerable attention in modern technologies due to their unique combination of catalytic activity, electro-chemical properties, and high specific surface area. Porous NiO is widely used as an active component or support in catalysts (for example, for the partial oxidation of methane, ammonia decomposition, and CO oxidation) [1], in gas sensors [2], electrodes for supercapacitors [3] and lithium-ion batteries [4], magnetic materials [5], as well as in photoelectrochemical devices [6–8]. The controlled formation of the NiO microstructure, particularly the parameters of porosity (pore size, pore size distribution, specific surface area, and total porosity), directly determines its functional performance in target applications.

One of the most effective and versatile approaches for the synthesis of porous oxide and metallic materials is the precursor method, which is based on the thermal decomposition of solid compounds with a predefined morphology [9,10]. This method enables the production of materials with reproducible microstructures and high purity. The thermal decomposition of nickel oxalate dihydrate ($NiC_2O_4{\cdot}2H_2O$) represents a particularly promising route because it allows the synthesis of both porous NiO (when decomposition occurs in an oxidizing atmosphere, e.g., in air) and porous metallic Ni (when decomposition takes place in an inert or reducing atmosphere, e.g., in hydrogen) [11–25]. Previous studies have demonstrated that the key parameters of the thermal decomposition process,

 doi:10.20944/preprints202603.1297.v1

namely the atmosphere, temperature, and holding time strongly influence the phase composition, morphology, and, most importantly, the characteristics of the porous structure of the final product.

It has been established that the phase composition of the final product formed during thermal decomposition strongly depends on the surrounding atmosphere. Under oxidizing conditions (air, O_2), nickel oxide (NiO) is consistently formed [12–25], whereas under purely reducing conditions (H_2), metallic nickel is obtained [16,25]. Metallic nickel can also be produced in an atmosphere containing N_2 + 20% CH_4 [15]. However, significant discrepancies remain regarding the nature of the decomposition products formed in inert atmospheres. In most studies carried out in N_2, Ar, and He, metallic Ni was reported as the sole decomposition product [13,26], although the formation of a mixture of Ni and NiO has also been suggested in several works [16,17,19,22,27].

Regardless of the atmosphere, the dehydration stage is always endothermic [11,17,23]. Dehydration of the precursor is often incomplete, and residual water may remain in the structure of anhydrous nickel oxalate (NiC_2O_4). This residual water can initiate secondary reactions during oxalate decomposition, leading to the formation of oxide phases [11,23]. During the decomposition stage of the oxalate anion, the process is endothermic in inert atmospheres (N_2, He, CO_2) and exothermic in oxidizing (air, O_2) or reducing (H_2) environments [16,17]. Moreover, the decomposition of nickel oxalate in air generally occurs at lower temperatures than in inert atmospheres or under vacuum [13,19,25].

The reaction product typically consists of porous microcontainers composed of nanosized primary particles [28,29]. The morphology of the precursor particles is preserved during the reaction, and the resulting products (NiO or Ni) may exhibit various morphologies that are determined at the precursor synthesis stage, such as nanoflakes or nanocubes [30–32]. This feature of the reaction forms the basis of the self-templated synthesis approach for NiO and Ni reported in several studies [9,10].

The formation of porosity during the thermal decomposition of $NiC_2O_4 \cdot 2H_2O$ is associated with the significant difference in molar volume between the precursor and the reaction product, as well as with the intensive evolution of gaseous products [11,25,29]. The specific surface area strongly depends on the composition of the gas atmosphere and the treatment temperature, since these factors determine the phase composition and the degree of nanoparticle sintering. During the thermal decomposition of oxalate in an oxidizing atmosphere (for example, in air), the main product is mesoporous nickel oxide (NiO). At relatively low temperatures, high values of specific surface area can be achieved. For example, at 300 °C a specific surface area of 179 m^2/g was reported [10]. However, increasing the reaction temperature to 340 °C leads to a significant decrease in the specific surface area to 79 m^2/g [10].

Decomposition in an inert atmosphere, such as pure nitrogen or argon, leads to the formation of metallic nickel (Ni). In [29], rapid decomposition in an argon flow at 612 °C produced nickel with a specific surface area ranging from 29 to 39 ± 4 m^2/g. In contrast, in an atmosphere containing hydrogen (5% H_2/Ar) at 612 °C, a lower specific surface area of S = 6.6 ± 0.6 m^2/g was observed compared with pure argon. This effect is attributed to the fact that the presence of hydrogen accelerates the sintering of metallic nickel particles [29]. The use of CH_4 as a reducing agent leads to the formation of a carbon film on the nickel particles, which effectively suppresses sintering and increases the specific surface area of the product [33].

During the thermal decomposition of mixed Fe(II) and Ni(II) oxalates in air aimed at producing nickel ferrite ($NiFe_2O_4$), materials with a higher specific surface area can be synthesized compared with those obtained from pure iron and nickel oxalates. For instance, a specific surface area of S = 335 m^2/g was achieved after thermal treatment at 500 °C for 1 h [34]. However, increasing the treatment time to 2 h at the same temperature reduces the specific surface area to 120 m^2/g due to the sintering of highly dispersed particles [34].

Despite the considerable number of studies devoted to the synthesis of NiO from nickel oxalate, several key issues remain unresolved. In particular, a detailed understanding of the mechanisms of pore formation and the identification of the main factors determining the parameters of the porous

 doi:10.20944/preprints202603.1297.v1

product under different conditions are still lacking. A deeper investigation of these aspects is necessary for the rational design of materials with tailored functional properties.

Therefore, the aim of the present work is to perform a comprehensive investigation of the thermal decomposition of nickel oxalate dihydrate as a precursor for the synthesis of porous NiO, with particular emphasis on the formation and evolution of microstructure. The specific objectives of this study are as follows:

1. To investigate the evolution of the microstructure during successive stages of the thermal decomposition reaction (dehydration and decomposition of the oxalate anion).
2. To analyze the mechanisms of pore formation and identify the key factors determining the parameters of the porous microstructure throughout the entire synthesis process and in the final product.

2. Materials and Methods

2.1. Precursor Preparation

Nickel oxalate dihydrate was prepared using two different methods. Chemically pure grade reagents (nickel sulfate heptahydrate, nickel nitrate dihydrate, ammonium oxalate monohydrate, potassium oxalate monohydrate, oxalic acid dihydrate, sodium silicate, sulfuric acid, and hydrochloric acid) were used as starting materials without further purification.

In the first case, the precursor (P1) was prepared by the precipitation method. For this purpose, 15 g of nickel sulfate heptahydrate was dissolved in 30 mL of distilled water acidified with sulfuric acid to pH = 1. 0.3 M ammonium oxalate solution was added dropwise to the resulting solution heated to T = 75 °C at a rate of 2 mL/min under constant stirring. The ammonium oxalate solution was added in 20% excess. After completion of the reaction, the hot suspension was filtered, washed with cold distilled water, and dried in air at 50 °C. The resulting blue–green powder of nickel oxalate dihydrate consisted of parallelepiped-shaped particles with sizes of 1–5 μm (Figure 1a).

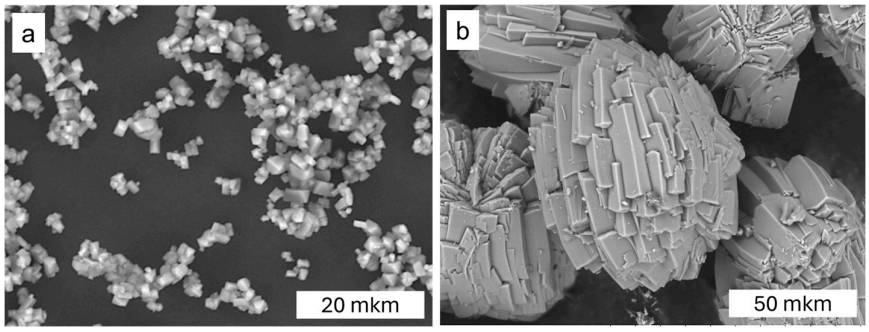

Figure 1. Nickel oxalate dihydrate samples obtained by (a) the precipitation method (P1) and (b) the counter-diffusion method in SiO_2 gel (P2).

In the second case, samples (P2) were obtained by the counter-diffusion method in a SiO_2 gel. A barrier layer of SiO_2 gel was formed in the lower part of a U-shaped tube as a result of the reaction between sodium silicate and hydrochloric acid. One arm of the tube contained 25 mL of 0.15 M nickel nitrate solution, while the other arm contained 25 mL of a mixture (1:1) of 0.08 M potassium oxalate solution and 0.09 M oxalic acid solution. After aging at T = 75 °C for seven days, isometric crystal aggregates with sizes ranging from 50 to 100 μm were formed (Figure 1b).

Samples of the P1 series were used in all experiments related to the synthesis and investigation of the properties of nickel oxide. The P2 series was obtained to provide a clearer visualization of the morphological changes occurring during the decomposition of the precursor.

 doi:10.20944/preprints202603.1297.v1

2.2. Sample Preparation and Characterization

Dehydration of the precursor in this work was carried out in air at a temperature of 175 °C for six hours. Nickel oxide was obtained by thermal decomposition of anhydrous nickel oxalate in air at 250 °C for 45 hours.

The samples were investigated using scanning electron microscopy (SEM, TM-1000 (Hitachi, Japan), 3400N (Hitachi, Japan)) and transmission electron microscopy (TEM, JEM-2200 FS, Japan).

Powder X-ray diffraction patterns of the obtained samples were recorded on a D8 Advance powder diffractometer (Bruker, Germany) with Bragg–Brentano geometry using Cu–Kα radiation and a LynxEye one-dimensional detector with a nickel filter (step size $\Delta 2\theta = 0.0195°$ and counting time of 0.2 s per step). In situ diffraction studies were carried out in an HTK 1200 N high-temperature chamber, where the temperature stability was ±0.1 °C, and the sample holder was an Al_2O_3 cuvette. Heating was performed at a rate of 5 °C/min with a holding time of 10 minutes before the start of data acquisition. Data collection was performed in the range of 10–60° for 25 and 250 °C and 20–80° for 350 and 500 °C. X-ray phase analysis of the samples was carried out using the PDF-4 database (ICDD, Release 2011). The unit cell parameters and crystallite sizes were determined by the Rietveld method using Topas 4.2 software (Bruker AXS, Germany). Visualization of structural data was carried out using Mercury 4.2.0 software [35].

The specific surface area of the obtained materials was determined from nitrogen adsorption–desorption isotherms measured at −196 °C using an ASAP 2020 instrument (Micromeritics, USA).

Synchronous thermogravimetric and differential scanning calorimetry analysis combined with mass spectrometry (TG–DSC–MS) was carried out using a NETZSCH STA-449F1 instrument (NETZSCH, Germany) with a heating rate of 5 K/min in an argon–oxygen mixture (80% Ar + 20% O_2). Analysis of evolved gases was per-formed using a QMS 403C Aëolos quadrupole mass spectrometer operating in multi-ion detection mode.

3. Results and Discussion

3.1. XRD, Thermal, and Mass Spectrometry Analyses

Nickel oxalate dihydrate, similarly to iron and cobalt oxalate dihydrates, crystallizes in two polymorphic modifications: a high-temperature monoclinic form (α phase) and a low-temperature orthorhombic form (β phase) [36]. Structurally, nickel oxalate dihydrate is a coordination polymer in which the oxalate anion ($C_2O_4^{2-}$) acts as a bidentate chelating ligand. All four oxygen atoms coordinate to nickel ions in a quasi-symmetric bidentate fashion, forming infinite chains (Figure 2, inset).

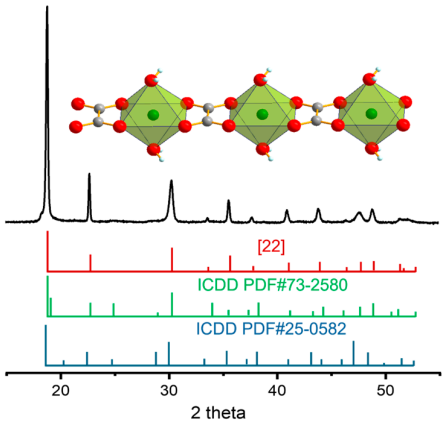

Figure 2. Powder XRD pattern of the precursor together with stick patterns corresponding to the α and β phases (ICDD PDF#73-2580 and 25-0582, respectively) and the disordered structure proposed in [22]. Inset: fragment of a nickel–oxalate chain in the precursor structure.

 doi:10.20944/preprints202603.1297.v1

The oxalate groups bridge adjacent nickel centers rather than forming terminal bonds; consequently, each oxalate anion forms two five-membered chelate rings rather than two four-membered rings. This bridging coordination mode results in a highly connected framework. Each Ni^{2+} ion is additionally coordinated by two water molecules, resulting in an octahedral coordination environment (Figure 2, inset). The coordinated water molecules form hydrogen bonds with oxalate groups of neighboring chains, thereby linking the chains into a three-dimensional structure. The α and β polymorphs differ in the packing arrangement of these chains.

The powder X-ray diffraction (XRD) pattern of the precursor synthesized in this work together with the stick patterns corresponding to the α (ICDD PDF#73-2580) and β (ICDD PDF#25-0582) phases are shown in Figure 2. Several reflections expected for these phases are absent in the experimental pattern. It has been previously reported [22] that increasing structural disorder in the monoclinic α phase leads to extinction of certain reflections in the powder pattern. This disorder can be interpreted as one-dimensional shifts of nickel–oxalate chains along the chain direction. Such shifts can be described by displacement vectors applied to the basis atoms and by the fraction of atoms involved in the displacement.

According to Ref. [22], the principal displacement vector is 0.4 along the [010] direction, while the fraction of displaced basis atoms is 0.405. The stick diagram corresponding to the disordered structure proposed in [22] is also shown in Figure 2. The diffraction pattern of the synthesized precursor agrees well with this model, indicating that the precursor possesses a disordered monoclinic structure.

The thermal decomposition of the precursor in a 20% O_2 / 80% Ar atmosphere was investigated using simultaneous thermogravimetry–differential scanning calorimetry–mass spectrometry (TG–DSC–MS) combined with in situ powder X-ray diffraction performed under identical heating conditions and gas atmosphere. This combined approach allows direct correlation between mass loss, thermal effects, gas evolution, and phase transformations occurring during the reaction. The TG–DSC curves (Figure 3) show that the decomposition proceeds in two main stages corresponding to dehydration followed by decomposition of the oxalate anion.

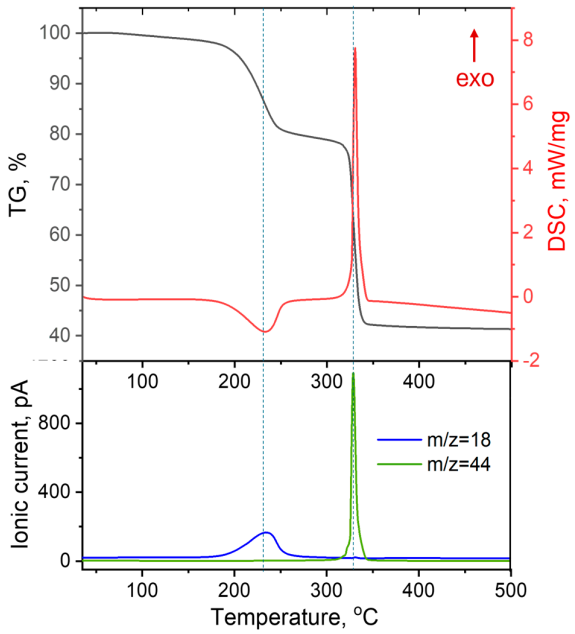

Figure 3. Results of simultaneous TG–DSC–MS analysis of the thermal decomposition of the precursor in an Ar–O_2 mixture (80% Ar + 20% O_2) at a heating rate of 5 °C min^{-1}.

The first mass-loss step occurs in the temperature range 100–275 °C and corresponds to removal of crystallization water. The observed mass loss (~20%) is in good agreement with the theoretical

 doi:10.20944/preprints202603.1297.v1

value expected for dehydration of nickel oxalate dihydrate (19.7%). This process is accompanied by an endothermic effect on the DSC curve. The simultaneously recorded MS signal shows a pronounced increase in the intensity of the m/z = 18 peak, confirming the evolution of water vapor (Figure 3). The in situ XRD patterns (Figure 4) indicate that the reflections of hydrated nickel oxalate disappear upon heating to 250 °C, while diffraction peaks corresponding to anhydrous nickel oxalate appear [22,23].

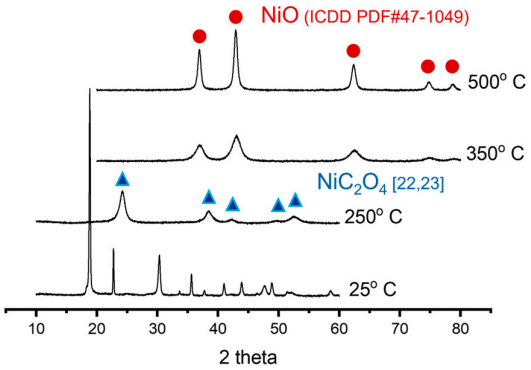

Figure 4. In situ powder XRD patterns recorded during thermal decomposition of the precursor in an Ar–O_2 atmosphere (80% Ar + 20% O_2).

No reflections corresponding to oxide phases are detected at this stage, confirming that the process corresponds exclusively to dehydration without decomposition of the oxalate anion. The reaction can therefore be described as

$$NiC_2O_4 \cdot 2H_2O \rightarrow NiC_2O_4 + 2H_2O \quad (1)$$

The second stage occurs between 300 and 350 °C and corresponds to decomposition of the oxalate group. The TG curve shows a total mass loss of approximately 59%, which is consistent with the formation of NiO (the theoretical value is 59.13%). Unlike decomposition in vacuum or inert atmospheres, this step is accompanied by a pronounced exothermic peak on the DSC curve, indicating participation of oxygen in the reaction. The simultaneously recorded MS spectra show strong signals at m/z = 44 corresponding to CO_2 evolution. The phase evolution observed by in situ powder XRD is consistent with these thermal analysis results. The diffraction peaks of nickel oxalate disappear, and new reflections corresponding to NiO appear at approximately 350 °C (Figure 4). The XRD patterns collected at 500 °C contain only reflections of NiO, confirming that nickel oxide is the final thermodynamically stable phase formed during decomposition of nickel oxalate under oxidative conditions. The second stage of the reaction can therefore be described by

$$NiC_2O_4 + 1/2O_2 \rightarrow NiO + 2CO_2 \quad (2)$$

Overall, the combined TG–DSC–MS and in situ powder XRD results demonstrate that the thermal decomposition of nickel oxalate proceeds via two sequential steps: dehydration of the hydrate followed by oxidative decomposition of the oxalate anion leading to the formation of NiO.

3.2. Microstructure Evolution during Dehydration: Fracture Mechanism

In the present work, dehydration of the precursor was performed in air at 175 °C for 6 h. The mass loss during this process was approximately 19.5%, corresponding to formation of anhydrous nickel oxalate. The diffraction pattern of the obtained sample is shown in Figure 5 and agrees well with that reported for the dehydration product in Ref. [22]. According to Ref. [22], the structure retains infinite cation–anion chains of the type –C_2O_4–Ni–C_2O_4–Ni–, while adjacent chains are linked

 doi:10.20944/preprints202603.1297.v1

through coordination of nickel atoms with oxygen atoms belonging to oxalate groups of neighboring chains (Figure 5, inset). Thus, removal of water molecules preserves the infinite chains but significantly reduces the distance between them, resulting in additional interchain bonding. The structural transformation from $NiC_2O_4{\cdot}2H_2O$ to NiC_2O_4 occurs in a temperature range where diffusion of entire NiC_2O_4 units through the lattice is strongly hindered. Consequently, the structural disorder present in the hydrate is inherited by the anhydrous oxalate. The stick diagram corresponding to the disordered structure proposed in Ref. [22] is also shown in Figure 5.

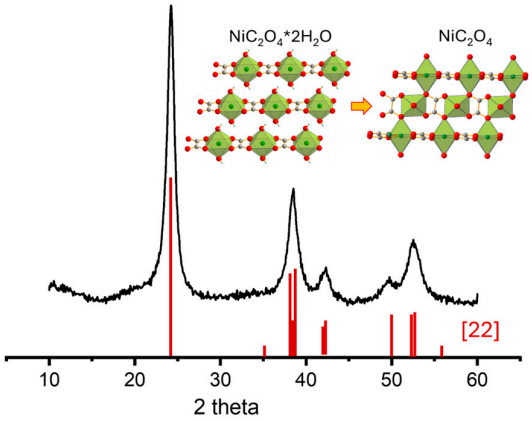

Figure 5. Powder XRD pattern of anhydrous nickel oxalate obtained by dehydration of nickel oxalate dihydrate together with the stick diagram corresponding to the structure reported in Ref. [22]. Inset: schematic representation of the structural transformation during dehydration.

Dehydration of nickel oxalate dihydrate is accompanied by a substantial decrease in volume, with a theoretical shrinkage of 42.6% [22]. The distance between nickel atoms along the chains changes only slightly (~3%), indicating that the volume change is mainly associated with a reduction of the interchain distance. Despite this large shrinkage, the morphology of the original crystals is preserved, although cracks appear on their surfaces (Figure 6). In literature this phenomenon has been described using various terms, including pseudomorphic conversion [37,38], shape-preserving conversion [39], morphology preservation [40], self-templated synthesis [9,41], and conformal transformation [42].

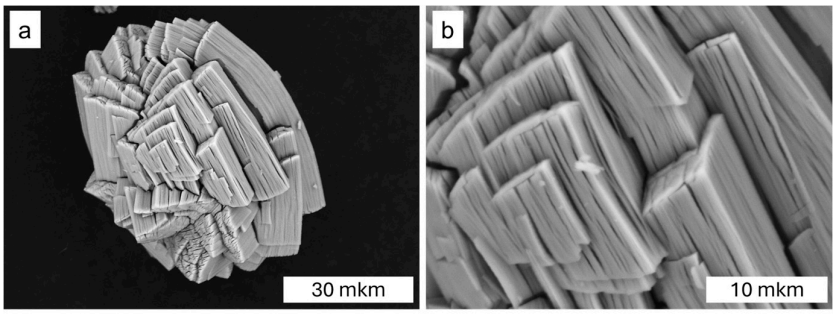

Figure 6. Pseudomorphic anhydrous nickel oxalate formed by dehydration of nickel oxalate dihydrate at different magnifications (a, b).

Preservation of the precursor morphology implies that mass transport during the re-action occurs over relatively short distances, while the reaction-induced volume change is accommodated by pores distributed throughout the pseudomorph. These pores may form either due to fracture associated with propagation of the reaction front or through diffusion-controlled pore growth.

 doi:10.20944/preprints202603.1297.v1

During dehydration, water molecules leave the crystal while the metal–oxalate chains forming the structural framework remain intact but move closer together and become interconnected. This structural rearrangement and the localization of the reaction near the reaction front generates mechanical stresses that lead to fracture. A general approach describing the influence of fracture on the kinetics and morphology of thermal decomposition reactions has been proposed in earlier studies [43–49]. Various aspects of this phenomenon have been examined, including mechanisms of structural transformation [44], anisotropy effects [45], reaction staging [46], formation of ordered structures [48], and the structure of the reaction front [49].

In the present work we consider the overall relationship between reaction and fracture during dehydration of nickel oxalate dihydrate. The reaction begins at the surface of the crystal, where water molecules are removed and a layer of reaction product forms. Because the product has a smaller volume and remains strongly bonded to the matrix, mechanical stresses develop within this layer. Once the elastic energy reaches a critical value, fracture occurs, generating a crack that becomes a new reaction surface. The reaction then occurs on the crack surface, creating a new reaction zone and generating additional stresses that lead to further cracking. Thus, the cycle of dehydration, stress accumulation, and fracture repeats periodically. As a result, the process proceeds via self-sustained propagation of a coupled reaction–fracture front, producing a uniformly fractured material behind the reaction front. The resulting particles remain interconnected by bridges of unbroken material, which provide residual mechanical strength and preserve the morphology of the precursor. The pores separating the particles correspond to crack cavities and form a connected network through which gaseous products escape. In this sense, the pores (cracks) may be considered as one of the products of the reaction, determining the microstructure of the resulting anhydrous oxalate. The propagation velocity of the reaction front and the characteristic fracture scale are stationary parameters determined by the coupled development of reaction and fracture. The fracture scale is controlled by the magnitude of deformation associated with the reaction shrinkage: larger shrinkage leads to smaller fracture scales.

Anisotropic shrinkage results in different fracture scales along different crystallo-graphic directions and therefore leads to the formation of anisotropic product particles [45]. Since during dehydration of $NiC_2O_4{\cdot}2H_2O$ the lattice parameter along the cation–anion chains changes only slightly, whereas the main shrinkage occurs perpendicular to these chains, fracture is expected to occur predominantly along the chain direction. Consequently, the product particles should exhibit an elongated morphology along this direction.

Indeed, Figure 6 shows parallel cracks aligned along the crystals forming the aggregate. The specific surface area of the resulting anhydrous oxalate determined by BET adsorption is 5–8 $m^2\ g^{-1}$. Based on this value, the approximate particle size forming the pseudomorph was estimated using the relation [50]:

$$d = \frac{K}{\rho \cdot S} \tag{3}$$

where d is the mean particle size, $\rho = 3.468$ g cm^{-3} is the density of the material, S is the specific surface area, and K is a shape factor accounting for particle morphology (K=4 for elongated particles (rods)). The estimated particle size ranges from 140 to 230 nm.

Thus, dehydration of $NiC_2O_4{\cdot}2H_2O$ proceeds via pseudomorphic conversion, resulting in the formation of submicron anisotropic particles separated by crack-like pores.

3.3. Mechanism of Pore Formation during Oxalate Decomposition

The thermal decomposition of anhydrous nickel oxalate in air was performed at 250 °C for 45 h. These conditions were selected to minimize the coarsening and sintering of nickel oxide nanoparticles formed during the reaction. The observed mass loss corresponds to the formation of NiO, while the broadened peaks in the X-ray powder diffraction pattern (Figure S1) indicate the formation of nanosized particles. During the reaction, a pseudomorphic transformation occurs, resulting in the

 doi:10.20944/preprints202603.1297.v1

formation of nano-crystalline nickel oxide (Figure 7a). The theoretical change in molar volume during the conversion of nickel oxalate to nickel oxide is 73.9%.

Samples of the obtained nickel oxide were examined using transmission electron mi-croscopy (Figure 7b). TEM results show that the nickel oxide particles have sizes of 2–4 nm. The specific surface area of nickel oxide determined by the BET method was 310–350 $m^2\ g^{-1}$. Assuming that the formed particles are isometric, their size can be estimated using (3) with $\rho(NiO)$ = 6.67 g cm^{-3} and K=6. The calculated particle size is 2.7 nm (for S = 330 $m^2\ g^{-1}$), which is in good agreement with the TEM data. The average crystallite size calculated from the analysis of the peak broadening of the product X-ray diffraction pattern is 4 nm (Figure S1).

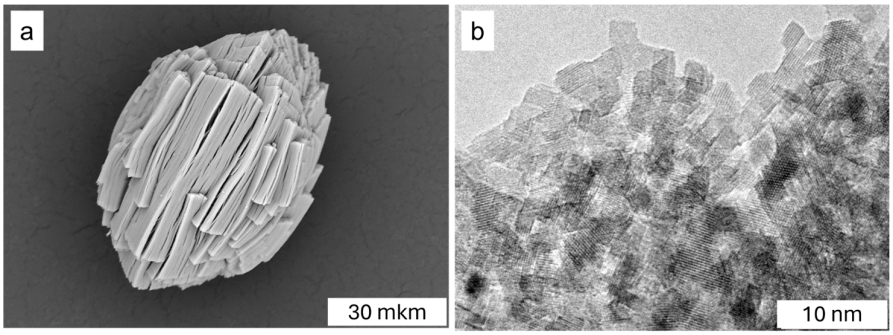

Figure 7. (a) Pseudomorph of nanocrystalline nickel oxide obtained during thermal decomposition of anhydrous nickel oxalate in air; (b) TEM image of nanocrystalline nickel oxide.

During dehydration of $NiC_2O_4{\cdot}2H_2O$, a pseudomorphic conversion occurs, resulting in submicron anisotropic particles separated by pore-cracks. These cracks permeate the entire pseudomorph volume and enable efficient removal of gaseous products during oxalate decomposition. Under such conditions, individual particles within the pseudomorph can react independently. As a result, the thermal decomposition of nickel oxalate proceeds uniformly throughout the entire pseudomorph volume. Therefore, the reaction mechanism can be analyzed by considering processes occurring within a single particle forming the pseudomorph generated after dehydration.

It is commonly assumed that the porosity formed during nickel oxalate decomposition arises from the large volume change associated with the reaction and from the evolution of gaseous products [11,25,29]. The decomposition reaction initiates at the particle surface with the cleavage of the C–C bond in the oxalate ion [51]. Subsequently, the Ni–O bond breaks, leading to the formation of two CO_2 molecules and a nickel atom. This process can be described by the following reaction:

$$NiC_2O_4 \rightarrow Ni + 2CO_2 \quad (4)$$

An alternative pathway has also been proposed in the literature:

$$NiC_2O_4 \rightarrow NiO + CO + CO_2 \quad (5)$$

However, analysis of experimental observations and theoretical calculations indicates that the pathway described by Equation (4) is thermodynamically more favorable [23,51].

Regardless of the specific reaction pathway, the transformation of oxalate ions into CO_2 and CO molecules disrupts the metal–oxalate chains and leads to the collapse of the crystalline framework of nickel oxalate. This process results in a significant structural rearrangement. The released nickel atoms initially form clusters that subsequently coalesce into metallic particles. Oxygen may react with individual atoms, clusters, or particles, converting them into NiO. The dominant pathway depends on the local concentration of adsorbed oxygen and on the rate of oxalate decomposition.

At 250 °C the decomposition proceeds relatively slowly (45 h), suggesting that oxidation occurs at the early stages of the reaction. If the pathway described by Equation (5) is realized, oxygen can

 doi:10.20944/preprints202603.1297.v1

additionally oxidize CO molecules. Oxidation of both metallic nickel and CO is highly exothermic and releases more heat than is required for oxalate decomposition. Therefore, in contrast to decomposition under vacuum or inert atmosphere, the reaction is accompanied by a pronounced exothermic peak in the DSC curve (Figure 3).

During the reaction, particles nucleate on the crystal surface and grow through the incorporation of nickel atoms from the surrounding region. Because the reaction leads to an almost fourfold reduction in volume, the material surrounding the growing particles becomes depleted, forming depressions that subsequently evolve into pores. The reaction proceeds on the pore surfaces, while nickel atoms or ions diffuse toward NiO particles forming the pore walls. As the reaction progresses, pores propagate into the crystal interior, forming a labyrinth-like structure that allows efficient removal of gaseous reaction products and access of oxygen.

This mechanism is similar to processes observed during the reduction of metal oxides [52,53] and during dealloying [54–56]. The particle and pore sizes are determined by the competition between the rate of oxalate decomposition at the pore surface and the diffusion mobility of nickel atoms or cations [52,53]. An increase in the reaction rate and/or a decrease in diffusion mobility leads to smaller particles and pores. Conversely, slower reaction kinetics and/or enhanced diffusion promote particle and pore growth.

In addition, the formed particles and pores may further grow due to coarsening and sintering driven by the reduction of surface energy. The rate of this process strongly depends on particle size and temperature and is controlled by the diffusion mobility [10,57]. To minimize this effect, the reaction should be performed at relatively low temperatures. Therefore, a synthesis temperature of 250 °C was selected in the present study. Under these conditions, exceptionally high specific surface areas were obtained compared with values reported in the literature. A schematic illustration of the transformation of nickel oxalate into NiO is shown in Figure 8.

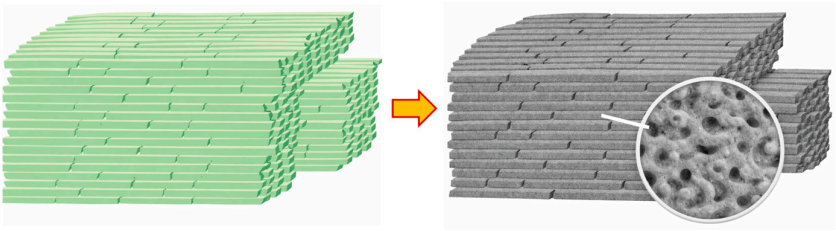

Figure 8. Illustration of the transformation of nickel oxalate into nickel oxide.

The proposed mechanism implies diffusion mobility of nickel atoms or cations. The relevant diffusion process occurs along the surface and at the reaction interface where the chemical transformation takes place. According to experimental observations in this study, the resulting NiO particles have sizes of 2–4 nm. Therefore, diffusion over distances of only several nanometers is sufficient to produce the observed microstructure.

The diffusion coefficient can be estimated using the relation $D \sim x^2/t^*$, where x is the diffusion length and t^* is the characteristic time of the diffusion process. This relation follows from the characteristic diffusion length $x \sim \sqrt{Dt^*}$ for non-steady diffusion processes [58]. In this case, the diffusion path x is comparable to the particle size h ($x \approx h$), while the characteristic diffusion time can be estimated as $t^* \sim h/V$, where V is the velocity of the reaction front. The reaction front velocity can be estimated by dividing the particle size after dehydration ($H \approx 200$ nm) by the total reaction time ($t = 45$ h). This yields $D \sim h \cdot H/t \sim 5 \times 10^{-21}$ m² s⁻¹.

Experimental data on the diffusion of nickel atoms or ions on the surface of nickel oxalate are not available. However, the estimated value can be compared with the surface diffusion coefficient of nickel on metallic Ni. According to literature data [59], the surface diffusion coefficient of nickel at 250 °C is in the range of 10^{-21}–10^{-19} m² s⁻¹. Although the defective oxalate surface formed during the reaction may enhance atomic mobility, interaction with oxygen may reduce diffusion rates. Nevertheless, the obtained estimate indicates that the proposed mechanism is physically plausible.

 doi:10.20944/preprints202603.1297.v1

The formation of gas bubbles and the associated pressure buildup inside crystals is expected only under extremely rapid heating conditions, such as rapid decomposition within an aerosol flow reactor [28,29]. In the present study the reaction was carried out at 250 °C for 45 h, making bubble formation inside crystals unlikely. Therefore, this mechanism can be neglected in the formation of porosity under the present experimental conditions.

To characterize the specific surface area and porosity of NiO and NiC_2O_4 samples, N_2 adsorption measurements were performed. The N_2 adsorption–desorption isotherms and corresponding pore size distributions calculated using the BJH model are shown in Figure S2. The hysteresis loop observed in the relative pressure range 0.4–0.9 is likely associated with pores between NiO nanoparticles. The high-pressure part of the hysteresis loop ($0.9 < P/P_0 < 1$) probably corresponds to larger textural pores formed during dehydration. The pore-size distribution (Figure S2, inset) shows a bimodal character, consisting of small mesopores (~3 nm) and larger macropores (~120 nm). Thus, the macroporous structure formed during dehydration is preserved in the final product, while mesopores are generated during oxalate decomposition. Since pseudomorph formation proceeds through multiple stages, pores are generated at each stage, resulting in a hierarchical pore structure (Figure 8).

4. Conclusions

Thermal decomposition of nickel oxalate dihydrate in air results in the formation of a porous structure that preserves the morphology of the initial particles and can be described as a pseudomorph. Since pseudomorph formation involves two stages—dehydration and oxalate decomposition—pore formation occurs during both stages of the reaction. A detailed mechanism of porosity formation at each stage is proposed. During dehydration, cracks divide the sample into blocks several hundred nanometers in size. During subsequent oxalate decomposition these blocks transform into mesoporous aggregates composed of nanosized particles. As a result, thermal decomposition of nickel oxalate in air produces a pseudomorphic NiO structure consisting of 2–4 nm nanoparticles and a hierarchical two-level pore system.

Many applications of NiO require both high reaction-accessible surface area and low transport resistance. Macropores reduce diffusion limitations, while mesopores increase the accessible surface area for adsorption and reaction. Therefore, materials possessing a hierarchical pore structure with macropores and interconnected mesoporous channels are promising for improving the performance of catalysts, sensors, supercapacitors, and Li-ion batteries.

Supplementary Materials: The following supporting information can be downloaded at the website of this paper posted on Preprints.org, Figure S1: Powder XRD pattern of NiO obtained by thermal decomposition of the precursor (250 °C, 45 h) together with stick patterns corresponding to ICDD PDF#47-1049.; Figure S2: Nitrogen adsorption and desorption isotherms of the NiO and NiC_2O_4. Inset: corresponding pore distribution derived from absorption data and calculated from the isotherm using the BJH model.

Author Contributions: Conceptualization, A.A.M., A.A.S.; methodology, A.A.M., A.A.S.; validation, M.M.K.; formal analysis, A.S.S., P.A.G.; investigation, A.S.S., A.A.M., P.A.G.; resources, A.S.S., U.K.M.; data curation, A.S.S. and A.A.M.; writing—original draft preparation, A.A.M. and A.S.S.; writing—review and editing, A.A.S., M.M.K.; visualization, A.A.M. and U.K.M. All authors have read and agreed to the published version of the manuscript

Funding: This research was carried out within the state assignment to ISSCM SB RAS (project No. 126021217268-2).

Data Availability Statement: The original contributions presented in this study are included in the article. Further inquiries can be directed to the corresponding author.

Conflicts of Interest: The authors declare no conflicts of interest.

 doi:10.20944/preprints202603.1297.v1

References

1. Dooley, K. M.; Chen, S. Y.; Ross, J. R. H. Stable Nickel-Containing Catalysts for the Oxidative Coupling of Methane. *Journal of Catalysis* **1994**, *145* (2), 402–408. https://doi.org/10.1006/jcat.1994.1050.
2. Mishra, S.; Yogi, P.; Sagdeo, P. R.; Kumar, R. Mesoporous Nickel Oxide (NiO) Nanopetals for Ultrasensitive Glucose Sensing. *Nanoscale Res Lett* **2018**, *13* (1), 16. https://doi.org/10.1186/s11671-018-2435-3.
3. Yan, H.; Zhang, D.; Xu, J.; Lu, Y.; Liu, Y.; Qiu, K.; Zhang, Y.; Luo, Y. Solution Growth of NiO Nanosheets Supported on Ni Foam as High-Performance Electrodes for Supercapacitors. *Nanoscale Res Lett* **2014**, *9* (1), 424. https://doi.org/10.1186/1556-276X-9-424.
4. Yang, H. X.; Dong, Q. F.; Hu, X. H.; Ai, X. P.; Li, S. X. Preparation and Characterization of $LiNiO_2$ Synthesized from $Ni(OH)_2$ and $LiOH{\cdot}H_2O$. *Journal of Power Sources* **1999**, *79* (2), 256–261. https://doi.org/10.1016/S0378-7753(99)00158-5.
5. Ichiyanagi, Y. Magnetic Properties of NiO Nanoparticles. *Physica B: Condensed Matter* **2003**, *329–333*, 862–863. https://doi.org/10.1016/S0921-4526(02)02578-4.
6. Awais, M.; Gibson, E.; Vos, J. G.; Dowling, D. P.; Hagfeldt, A.; Dini, D. Fabrication of Efficient NiO Photocathodes Prepared via RDS with Novel Routes of Substrate Processing for *p* -Type Dye-Sensitized Solar Cells. *ChemElectroChem* **2014**, *1* (2), 384–391. https://doi.org/10.1002/celc.201300178.
7. Sheehan, S.; Naponiello, G.; Odobel, F.; Dowling, D. P.; Di Carlo, A.; Dini, D. Comparison of the Photoelectrochemical Properties of RDS NiO Thin Films for P-Type DSCs with Different Organic and Organometallic Dye-Sensitizers and Evidence of a Direct Correlation between Cell Efficiency and Charge Recombination. *J Solid State Electrochem* **2015**, *19* (4), 975–986. https://doi.org/10.1007/s10008-014-2703-9.
8. Bonomo, M.; Naponiello, G.; Venditti, I.; Zardetto, V.; Carlo, A. D.; Dini, D. Electrochemical and Photoelectrochemical Properties of Screen-Printed Nickel Oxide Thin Films Obtained from Precursor Pastes with Different Compositions. *J. Electrochem. Soc.* **2017**, *164* (2), H137–H147. https://doi.org/10.1149/2.0051704jes.
9. Guo, L.; Arafune, H.; Teramae, N. Synthesis of Mesoporous Metal Oxide by the Thermal Decomposition of Oxalate Precursor. *Langmuir* **2013**, *29* (13), 4404–4412. https://doi.org/10.1021/la400323f.
10. Yu, C.; Zhang, L.; Shi, J.; Zhao, J.; Gao, J.; Yan, D. A Simple Template-Free Strategy to Synthesize Nanoporous Manganese and Nickel Oxides with Narrow Pore Size Distribution, and Their Electrochemical Properties. *Adv Funct Materials* **2008**, *18* (10), 1544–1554. https://doi.org/10.1002/adfm.200701052.
11. Chenakin, S.; Kruse, N. Thermal Decomposition of Nickel Oxalate Dihydrate: A Detailed XPS Insight. *J. Phys. Chem. C* **2019**, *123* (51), 30926–30936. https://doi.org/10.1021/acs.jpcc.9b07879.
12. Palanisamy, T.; Gopalakrishnan, J.; Viswanathan, B.; Srinivasan, V.; Sastri, M. V. C. Kinetics of Thermal Decomposition of Some Metal Oxalates. *Thermochimica Acta* **1971**, *2* (3), 265–273. https://doi.org/10.1016/0040-6031(71)85011-6.
13. Mansour, S. A. A. Spectroscopic and Microscopic Investigations of the Thermal Decomposition Course of Nickel Oxysalts. *Thermochimica Acta* **1993**, *230*, 243–257. https://doi.org/10.1016/0040-6031(93)80364-G.
14. Zhan, D.; Cong, C.; Diakite, K.; Tao, Y.; Zhang, K. Kinetics of Thermal Decomposition of Nickel Oxalate Dihydrate in Air. *Thermochimica Acta* **2005**, *430* (1–2), 101–105. https://doi.org/10.1016/j.tca.2005.01.029.
15. Mu, J.; Perlmutter, D. D. Thermal Decomposition of Carbonates, Carboxylates, Oxalates, Acetates, Formates, and Hydroxides. *Thermochimica Acta* **1981**, *49* (2–3), 207–218. https://doi.org/10.1016/0040-6031(81)80175-X.
16. Mohamed, M. A.; Galwey, A. K.; Halawy, S. A. A Comparative Study of the Thermal Reactivities of Some Transition Metal Oxalates in Selected Atmospheres. *Thermochimica Acta* **2005**, *429* (1), 57–72. https://doi.org/10.1016/j.tca.2004.08.021.
17. Dollimore, D.; Griffiths, D. L.; Nicholson, D. 488. The Thermal Decomposition of Oxalates. Part II. Thermogravimetric Analysis of Various Oxalates in Air and in Nitrogen. *J. Chem. Soc.* **1963**, 2617. https://doi.org/10.1039/jr9630002617.
18. Broadbent, D.; Dollimore, D.; Dollimore, J. The Thermal Decomposition of Oxalates. Part V. The Thermal Decomposition of Nickel Oxalate Dihydrate. *J. Chem. Soc., A* **1966**, 278. https://doi.org/10.1039/j19660000278.

 doi:10.20944/preprints202603.1297.v1

19. Macklen, E. D. Influence of Atmosphere on the Thermal Decomposition of Some Transition Metal Oxalates. *Journal of Inorganic and Nuclear Chemistry* **1968**, *30* (10), 2689–2695. https://doi.org/10.1016/0022-1902(68)80396-3.
20. Nikumbh, A. K.; Athare, A. E.; Raut, V. B. A Study of the Thermal Decomposition of Cobalt(II) and Nickel(II) Oxalate Dihydrate Using Direct Current Electrical Conductivity Measurements. *Thermochimica Acta* **1991**, *186* (2), 217–233. https://doi.org/10.1016/0040-6031(91)87038-X.
21. Majumdar, R.; Sarkar, P.; Ray, U.; Roy Mukhopadhyay, M. Secondary Catalytic Reactions during Thermal Decomposition of Oxalates of Zinc, Nickel and Iron(II). *Thermochimica Acta* **1999**, *335* (1–2), 43–53. https://doi.org/10.1016/S0040-6031(99)00128-8.
22. Puzan, A. N.; Baumer, V. N.; Lisovytskiy, D. V.; Mateychenko, P. V. Structure Transformations in Nickel Oxalate Dihydrate $NiC_2O_4{\cdot}2H_2O$ and Nickel Formate Dihydrate $Ni(HCO_2)_2{\cdot}2H_2O$ during Thermal Decomposition. *Journal of Solid State Chemistry* **2018**, *266*, 133–142. https://doi.org/10.1016/j.jssc.2018.07.005.
23. Małecka, B.; Małecki, A.; Drożdż-Cieśla, E.; Tortet, L.; Llewellyn, P.; Rouquerol, F. Some Aspects of Thermal Decomposition of $NiC_2O_4{\cdot}2H_2O$. *Thermochimica Acta* **2007**, *466* (1–2), 57–62. https://doi.org/10.1016/j.tca.2007.10.010.
24. Drożdż-Cieśla, E.; Wyrwa, J.; Broś, J.; Rękas, M. Structural, Microstructural, Thermal, and Electrical Properties of Ni/YSZ Cermet Materials. *J Therm Anal Calorim* **2012**, *108* (3), 1051–1057. https://doi.org/10.1007/s10973-012-2281-y.
25. Dollimore, D. The Thermal Decomposition of Oxalates. A Review. *Thermochimica Acta* **1987**, *117*, 331–363. https://doi.org/10.1016/0040-6031(87)88127-3.
26. Shen, B. R.; Shen, H.; Pan, Y. X.; Che, T. F.; Cai, X. E. The Thermal Decomposition of $NiC_2O_4{\cdot}2H_2O$: An In Situ TP-XRD and TGA/FT-IR Study. *Z. Phys. Chem.* **2001**, *215*, 1413–1418.
27. Yong, W. J.; Hall, B. The Thermal Decomposition of Nickel Oxalates Doped with Traces of Other Metal Ions. *Thermochimica Acta* **1989**, *147* (2), 251–260. https://doi.org/10.1016/0040-6031(89)85180-9.
28. Carney, C. S.; Gump, C. J.; Weimer, A. W. Rapid Nickel Oxalate Thermal Decomposition for Producing Fine Porous Nickel Metal Powders. *Materials Science and Engineering: A* **2006**, *431* (1–2), 1–12. https://doi.org/10.1016/j.msea.2006.04.036.
29. Carney, C. S.; Gump, C. J.; Weimer, A. W. Rapid Nickel Oxalate Thermal Decomposition for Producing Fine Porous Nickel Metal Powders. *Materials Science and Engineering: A* **2006**, *431* (1–2), 26–40. https://doi.org/10.1016/j.msea.2006.04.038.
30. Bonomo, M. Synthesis and Characterization of NiO Nanostructures: A Review. *J Nanopart Res* **2018**, *20* (8), 222. https://doi.org/10.1007/s11051-018-4327-y.
31. Rakshit, S.; Chall, S.; Mati, S. S.; Roychowdhury, A.; Moulik, S. P.; Bhattacharya, S. C. Morphology Control of Nickel Oxalate by Soft Chemistry and Conversion to Nickel Oxide for Application in Photocatalysis. *RSC Adv.* **2013**, *3* (17), 6106. https://doi.org/10.1039/c3ra21978j.
32. Vaidya, S.; Rastogi, P.; Agarwal, S.; Gupta, S. K.; Ahmad, T.; Antonelli, A. M.; Ramanujachary, K. V.; Lofland, S. E.; Ganguli, A. K. Nanospheres, Nanocubes, and Nanorods of Nickel Oxalate: Control of Shape and Size by Surfactant and Solvent. *J. Phys. Chem. C* **2008**, *112* (33), 12610–12615. https://doi.org/10.1021/jp803575h.
33. Wang, H. Y.; Lua, A. C. Development of Metallic Nickel Nanoparticle Catalyst for the Decomposition of Methane into Hydrogen and Carbon Nanofibers. *J. Phys. Chem. C* **2012**, *116* (51), 26765–26775. https://doi.org/10.1021/jp306519t.
34. Hayrapetyan, S. S.; Khachatryan, H. G. The Porosity of Partly Sintered Nickel Iron Oxalates. *Microporous and Mesoporous Materials* **2006**, *89* (1–3), 33–38. https://doi.org/10.1016/j.micromeso.2005.06.045.
35. Macrae, C. F.; Sovago, I.; Cottrell, S. J.; Galek, P. T. A.; McCabe, P.; Pidcock, E.; Platings, M.; Shields, G. P.; Stevens, J. S.; Towler, M.; Wood, P. A. *Mercury 4.0* : From Visualization to Analysis, Design and Prediction. *J Appl Crystallogr* **2020**, *53* (1), 226–235. https://doi.org/10.1107/S1600576719014092.
36. Deyrieux, R.; Berro, C.; Peneloux, A. Studies on Oxalates of Some Bivalent Metals- Crystal-Structure of Dihydrated Manganese, Cobalt, Nickel and Zinc Oxalates- Polymorphism of Dihydrated Cobalt and Nickel Oxalates. *Bull. Soc. Chim. Fr* **1973**, *12*, 25–34.

 doi:10.20944/preprints202603.1297.v1

37. Popa, K.; Walter, O.; Blanco, O. D.; Guiot, A.; Bouëxière, D.; Colle, J.-Y.; Martel, L.; Naji, M.; Manara, D. A Low-Temperature Synthesis Method for AnO_2 Nanocrystals (An = Th, U, Np, and Pu) and Associate Solid Solutions. *CrystEngComm* **2018**, *20* (32), 4614–4622. https://doi.org/10.1039/C8CE00446C.
38. McDonald, L. W.; Sentz, K.; Hagen, A.; Chung, B. W.; Nizinski, C. A.; Schwerdt, I. J.; Hanson, A.; Donald, S.; Clark, R.; Sjoden, G.; Porter, R.; Athon, M. T.; Tasdizen, T.; Noel, V.; Webb, S. M.; Van Veelen, A.; Hickam, S. M.; Ly, C. Review of Multi-Faceted Morphologic Signatures of Actinide Process Materials for Nuclear Forensic Science. *Journal of Nuclear Materials* **2024**, *588*, 154779. https://doi.org/10.1016/j.jnucmat.2023.154779.
39. Hendrikse, H. C.; Hémon-Charles, S.; Helmbrecht, L.; Van Dam, E. P.; Garnett, E. C.; Noorduin, W. L. Shaping Tin Nanocomposites through Transient Local Conversion Reactions. *Crystal Growth & Design* **2021**, *21* (8), 4500–4505. https://doi.org/10.1021/acs.cgd.1c00393.
40. Angermann, A.; Töpfer, J. Synthesis of Magnetite Nanoparticles by Thermal Decomposition of Ferrous Oxalate Dihydrate. *J Mater Sci* **2008**, *43* (15), 5123–5130. https://doi.org/10.1007/s10853-008-2738-3.
41. Liu, Y.; Fan, D.; Liu, B. Strategies for Template-Free Synthesis of Mesoporous Metal Catalysts with Surface-Clean Sites. *Acc. Mater. Res.* **2025**, *6* (10), 1246–1255. https://doi.org/10.1021/accountsmr.5c00164.
42. Galarneau, A.; Iapichella, J.; Bonhomme, K.; Di Renzo, F.; Kooyman, P.; Terasaki, O.; Fajula, F. Controlling the Morphology of Mesostructured Silicas by Pseudomorphic Transformation: A Route Towards Applications. *Adv Funct Materials* **2006**, *16* (13), 1657–1667. https://doi.org/10.1002/adfm.200500825.
43. Chupakhin, A. P.; Sidel'nikov, A. A.; Boldyrev, V. V. Control of the Reactivity of Solids by Changing Their Mechanical Properties. *Reactivity of Solids* **1987**, *3* (1–2), 1–19. https://doi.org/10.1016/0168-7336(87)80013-X.
44. Matvienko, A. A.; Chizhik, S. A.; Sidel'nikov, A. A. A New Kinetic Model of Calcite Thermal Decomposition. *Dokl Phys Chem* **2013**, *451* (2), 184–186. https://doi.org/10.1134/S001250161308006X.
45. Matvienko, A. A.; Chizhik, S. A.; Sidel'nikov, A. A. Factors Controlling the Morphology of the Surface of $BaC_2O_4{*}H_2C_2O_4{*}2H_2O$ during Its Dehydration. *Russ. J. Phys. Chem. A* **2005**, *79*, 1478–1482.
46. Yatsenko, D. A.; Pakharukova, V. P.; Tsybulya, S. V.; Matvienko, A. A.; Sidel'nikov, A. A. Phase Composition and Structure of Nanocrystalline Products of Solid-Phase Oxidative Thermolysis of Iron Oxalate Dihydrate. *J Struct Chem* **2012**, *53* (3), 548–556. https://doi.org/10.1134/S0022476612030195.
47. Chizhik, S.; Sidelnikov, A. The Kinetics of Solid State Reactions Accompanied by Fracture: II. Model of Stationary Front with Disordered Fracture Morphology. *Solid State Ionics* **2007**, *178* (27–28), 1487–1492. https://doi.org/10.1016/j.ssi.2007.09.010.
48. Chizhik, S.; Sidelnikov, A. The Kinetics of Solid State Reactions Accompanied by Fracture: III. Model of Stationary Front with Spatially Ordered Fracture Morphology. *Solid State Ionics* **2008**, *179* (33–34), 1823–1834. https://doi.org/10.1016/j.ssi.2008.05.002.
49. Chizhik, S.; Matvienko, A.; Sidelnikov, A. Spatially-Ordered Nano-Sized Crystallites Formed by Dehydration-Induced Single Crystal Cracking of $CuCl_2{\cdot}2H_2O$. *CrystEngComm* **2018**, *20* (39), 6005–6017. https://doi.org/10.1039/C8CE00683K.
50. Gregg, S. J.; Sing, K. S. W. *Adsorption, Surface Area, and Porosity*, 2nd ed.; Academic Press: London ; New York, 1982; pp. 30-36.
51. Koleżyński, A.; Handke, B.; Drożdż-Cieśla, E. Crystal Structure, Electronic Structure, and Bonding Properties of Anhydrous Nickel Oxalate. *J Therm Anal Calorim* **2013**, *113* (1), 319–328. https://doi.org/10.1007/s10973-012-2844-y.
52. Hayes, P. C. Analysis of Product Morphologies and Reaction Mechanisms on Gaseous Reduction of Iron Oxides. *steel research int.* **2011**, *82* (5), 480–493. https://doi.org/10.1002/srin.201100032.
53. Hidayat, T.; Rhamdhani, M. A.; Jak, E.; Hayes, P. C. On the Relationships between the Kinetics and Mechanisms of Gaseous Hydrogen Reduction of Solid Nickel Oxide. *Metall Mater Trans B* **2009**, *40* (4), 474–489. https://doi.org/10.1007/s11663-009-9239-x.
54. Erlebacher, J.; Aziz, M. J.; Karma, A.; Dimitrov, N.; Sieradzki, K. Evolution of Nanoporosity in Dealloying. *Nature* **2001**, *410* (6827), 450–453. https://doi.org/10.1038/35068529.
55. Erlebacher, J.; Sieradzki, K. Pattern Formation during Dealloying. *Scripta Materialia* **2003**, *49* (10), 991–996. https://doi.org/10.1016/S1359-6462(03)00471-8.

 doi:10.20944/preprints202603.1297.v1

56. Chen, Q.; Sieradzki, K. Mechanisms and Morphology Evolution in Dealloying. *J. Electrochem. Soc.* **2013**, *160* (6), C226–C231. https://doi.org/10.1149/2.064306jes.
57. Bordia, R. K.; Camacho-Montes, H. Sintering: Fundamentals and Practice. In *Ceramics and Composites Processing Methods*; Bansal, N. P., Boccaccini, A. R., Eds.; Wiley, 2012; pp. 1–42. https://doi.org/10.1002/9781118176665.ch1.
58. Shewmon, P. *Diffusion in Solids*, 2nd ed.; Springer: Cham, 2016; pp. 14-26. https://doi.org/10.1007/978-3-319-48206-4.
59. Maiya, P. S.; Blakely, J. M. Surface Self-Diffusion and Surface Energy of Nickel. *Journal of Applied Physics* **1967**, *38* (2), 698–704. https://doi.org/10.1063/1.1709399.